

# Electric-Field Control of Magnetic Skyrmion Chirality in a Centrosymmetric 2D

van der Waals Magnet

Myung-Geun Han<sup>1\*</sup>, Joachim Dahl Thomsen<sup>2,3\*</sup>, John P. Philbin<sup>3</sup>, Junsik Mun<sup>1</sup>,  
Eugene Park<sup>2</sup>, Fernando Camino<sup>4</sup>, Lukáš Děkánovský<sup>5</sup>, Chuhang Liu<sup>1,6</sup>, Zdenek  
Sofer<sup>5</sup>, Prineha Narang<sup>3</sup>, Frances M. Ross<sup>2</sup> and Yimei Zhu<sup>1</sup>

<sup>1</sup>Condensed Matter Physics and Materials Science, Brookhaven National Laboratory, Upton,  
New York 11973, USA

<sup>2</sup>Department of Materials Science and Engineering, Massachusetts Institute of Technology,  
Cambridge, Massachusetts 02139, USA

<sup>3</sup>Division of Physical Sciences, College of Letters and Science, University of California, Los  
Angeles, California 90095, USA

<sup>4</sup>Center for Functional Nanomaterials, Brookhaven National Laboratory, Upton, New York  
11973, USA

<sup>5</sup>Department of Inorganic Chemistry, University of Chemistry and Technology Prague,  
Technická 5, Prague 6, 166 28, Czech Republic

<sup>6</sup>Department of Physics and Astronomy, Stony Brook University, Stony Brook, New York  
11794, USA

These authors contributed equally: Myung-Geun Han, Joachim Dahl Thomsen

\*Email: [mghan@bnl.gov](mailto:mghan@bnl.gov)

## **Abstract**

Two-dimensional van der Waals magnets hosting topological magnetic textures, such as skyrmions, show promise for applications in spintronics and quantum computing. Electrical control of these topological spin textures would enable novel devices with enhanced performance and functionality. Here, using electron microscopy combined with *in situ* electric and magnetic biasing, we show that the skyrmion chirality, whether left-handed or right-handed, in insulating  $\text{Cr}_2\text{Ge}_2\text{Te}_6$ , is controlled by external electric field direction applied during magnetic field cooling process. The electric-field-tuned chirality remains stable, even amid variations in magnetic and electric fields. Our theoretical investigation reveals that nonzero Dzyaloshinskii-Moriya interactions between the nearest neighbors, induced by the external electric field, change their sign upon reversing the electric field direction, thereby facilitating chirality selection. The electrical control of magnetic chirality demonstrated in this study can be extended to other non-metallic centrosymmetric skyrmion-hosting magnets, opening avenues for future device designs in topological spintronics and quantum computing.

## **Main text**

Magnetic skyrmions and topologically nontrivial spin structures in two-dimensional (2D) van der Waals (vdW) materials have been studied extensively, driven by interest in fundamental spin physics in low dimensions and potential spintronic applications.<sup>1-3</sup> These topologically protected spin structures exhibit particle-like stability, making them potential information carriers in spintronic devices<sup>4</sup>. In 2D vdW materials, the integration of skyrmions with other 2D vdW layers featuring diverse and tunable physical properties presents enticing opportunities for designing novel states with emergent properties and behaviors.<sup>5-7</sup> Topological spin structures have been experimentally reported in various 2D vdW ferromagnetic materials, including skyrmionic bubbles in  $\text{Cr}_2\text{Ge}_2\text{Te}_6$  (CGT)<sup>8</sup> with perpendicular uniaxial anisotropy, and Néel-type skyrmions in oxidized  $\text{Fe}_3\text{GeTe}_2$ <sup>9</sup> and  $\text{WTe}_2/\text{Fe}_3\text{GeTe}_2$ .<sup>10</sup> There are two primary types of skyrmions in ferromagnetic 2D vdW magnets, based on their stabilization mechanisms: one with Dzyaloshinskii-Moriya interaction (DMI) and the other without DMI. By analogy to bulk chiral magnets,<sup>11</sup> nonzero DMI in non-centrosymmetric crystal structures stabilizes chiral spin arrangements.<sup>12</sup> The chirality of DMI-stabilized skyrmions is strongly coupled to the crystal structure. Conversely, in centrosymmetric crystals with uniaxial anisotropy, such as CGT,<sup>8</sup> dipolar interactions serve to stabilize Bloch-type skyrmionic bubbles. These Bloch-type skyrmionic bubbles are topologically equivalent to the Bloch-type skyrmions in chiral magnets. However, due to the absence of DMIs, the chirality of the skyrmionic bubbles in centrosymmetric magnets is random.

The ability to control the chirality of skyrmionic spin structures by electric means is pivotal for realizing spintronic applications and designing novel states in 2D heterostructures<sup>13-15</sup> and quantum computing applications.<sup>16</sup> For example, in the topological Hall effect, the interaction between the skyrmions and the conduction electrons depends on the chirality of the skyrmions.<sup>11</sup>

Thus, deterministic control of skyrmion chirality can provide a viable way to exploit the emergent electromagnetic dynamics of skyrmions, in addition to the electron transport properties. We note that electric fields can polarize insulating ferromagnetic 2D vdW materials. In a polarized state, nonzero DMIs may arise as the centrosymmetry is broken. Furthermore, as the sign of electric-field-induced DMIs is switchable by reversing the direction of the electric field, the magnetic chirality of the skyrmionic spin structures in insulating or semiconducting 2D ferromagnets can be controlled by electric field. In fact, a few theoretical studies have predicted that out-of-plane electric fields can induce skyrmionic spin structures in insulating 2D vdW  $\text{CrI}_3$  ( $\sim 1$  eV bandgap<sup>17</sup>) monolayer<sup>18-19</sup> and CGT ( $\sim 0.4$  eV bandgap<sup>20</sup>) heterostructures.<sup>21</sup> Additionally, the magnetic properties of CGT can be manipulated with electric stimuli. For instance, electrogating experiments performed on CGT layers with an ionic gel showed not only a dramatic increase in  $T_C$  (from 60 K to 200 K), but also an easy axis rotation from out-of-plane to in-plane direction, leading to a significant change in magnetic spin structures.<sup>22</sup> A recent study showed that the spin helicity in a metallic helimagnet MnP can be controlled by spin-transfer torque when the current direction is parallel to the external magnetic field applied.<sup>23</sup> Nevertheless, there has been no experimental work on the control of topological magnetic spin structures by external electric fields in insulating or semiconducting 2D vdW magnets.

In this report, by integrating *in situ* electric and magnetic fields with cryogenic Lorentz transmission electron microscopy (LTEM), we demonstrate experimentally the tunable chirality of skyrmionic bubbles in CGT flakes. Our data show that the vorticity (the direction of in-plane spin rotation) of Bloch-type skyrmionic bubbles was reversed by changing the electric field direction without any change in the polarity (the core spin direction), favoring one of the two possible chiralities by an external electric field. Our density functional theory calculation supports

these experimental observations, attributing the chirality selection in skyrmionic bubbles to the electric-field-induced DMIs between the nearest neighbors. Achieving chirality control by an electric field, as experimentally demonstrated in this study, opens up promising avenue for designing novel spintronic devices based on topological spin structures in the 2D vdW heterostructures.

Figure 1a shows a few-layer graphene (FLG)/CGT/FLG heterostructure fabricated over an electron-beam imaging window (vacuum) that was patterned in a custom designed silicon nitride membrane chip with two pre-patterned electrodes (Norcada Inc., Fig. S1 in the Supplementary Information). As the CGT has a bandgap ( $\sim 0.4$  eV), no large current is expected to flow through the heterostructure, especially at low temperatures where thermally excited carriers are quenched. To ensure a low leakage current flowing through the heterostructure and avoid Joule heating, we also fabricated heterostructures with an additional insulator layer, composed of FLG/hexagonal boron nitride (*h*BN)/CGT/FLG (Fig. S2). The resistance measured during cooling under a constant voltage 1 V (Fig. 1c) in the FLG/CGT/FLG sample shows an increase in the resistance with decreasing temperature, a characteristic insulator behavior. As shown in the inset of Fig. 1c, a local minimum in the resistance gradient at  $T \sim 55$  K occurs close to the  $T_C$ , indicating a link between magnetic spin structures and electrical transport properties.

Fig. 1d shows an over-focused LTEM image taken after 50 mT magnetic field cooling in the absence of an electric field. Hexagonally-close-packed skyrmionic bubbles with  $\sim 150$  nm diameter were observed, as reported in our previous study.<sup>8</sup> When the exfoliated flakes are imaged along the *c*-axis, the bubble core (magnetization direction up) and peripheral (magnetization direction down) spin components do not generate any contrast in the LTEM imaging as they are in the imaging direction. Instead, the visible LTEM contrast comes from the Bloch walls where the

magnetic spins are perpendicular to the direction of imaging electrons, as reported in previous LTEM studies.<sup>8,24</sup> Based on the magnetic contrast in Fig. 1d, two distinguishable skyrmionic bubbles can be identified, as marked with the blue and red boxes. In an over-focus imaging condition, a CCW skyrmionic bubble displays a dark-to-bright contrast from the perimeter to the core due to the Lorentz-force-induced converging electron beams. Conversely, for a CW skyrmionic bubble, the contrast is reversed to bright-to-dark due to the diverging electron beams. As the LTEM contrast also reverses when transitioning from underfocus to overfocus (Fig. S3), to determine chirality of skyrmionic bubbles, we primarily utilized overfocus imaging. Here, all skyrmionic bubbles have their core spin direction antiparallel to the applied magnetic field. Thus, the polarity (P) of skyrmionic bubbles is always positive (+P), as schematically shown in Fig. 1e. The vorticity is defined as the in-plane rotation sense, either clockwise (CW) or anticlockwise (CCW), within the Bloch walls that separate the core domain from the peripheral domain. Consequently, the chirality of skyrmionic bubbles is determined to be either right-handed or left-handed, depending on both polarity and vorticity (Figs. 1e). As the polarity in skyrmionic bubbles is fixed in our experiment, the vorticity solely determines the chirality; CCW is associated with the right-handed skyrmionic bubble while CW corresponds to left-handed, which was confirmed by micromagnetic simulations and LTEM contrast simulations, as shown in Fig. 1e. In our micromagnetic simulations, the right-handed and left-handed skyrmionic bubbles are induced by negative and positive bulk DMIs ( $\pm 1.25 \times 10^{-4} \text{ J/m}^2$ ), respectively.

To study electric field effects on the skyrmionic bubble chirality, we applied various electric fields during separate cooling processes from  $T > 80 \text{ K}$  to  $12 \text{ K}$  through  $T_C$  under a constant magnetic field (50 mT). After completion of the cooling process, the magnetic field was reduced to a residual value, which is  $\sim 11 \text{ mT}$  inside our electron microscope.<sup>8</sup> Note that the electric and

magnetic field directions are parallel to the crystallographic  $c$ -axis and the imaging direction in the electron microscope (see Fig. 1b). We define positive electric field direction as parallel to the imaging direction, and negative as antiparallel. Figure 2a–b shows LTEM images of the FLG/CGT/FLG heterostructure taken at  $T = 14$  K after the 50 mT magnetic field cooling with simultaneous application of positive and negative 18 mV/nm electric fields, respectively. Based on the LTEM image contrast of each bubble, which exhibited either bright-to-dark or dark-to-bright transitions from the perimeter to the core, we find that the negative electric field induced CCW skyrmionic bubbles (Fig. 2a), while the positive electric field induced CW bubbles. This demonstrates that the chirality of skyrmionic bubbles has been selectively controlled by an external electric field throughout the field cooling process. As shown in Fig. 2c, attempts to reverse the chirality of the CW skyrmionic bubbles (Fig. 2b) by applying a negative electric field up to 36 mV/nm at 16 K, far below  $T_C$ , resulted in sample damage. The application of such a high electric field caused Joule heating, leading to a significant alteration in the magnetic domain structure characterized by coexisting stripe domains and skyrmionic bubbles (Fig. 2c), suggesting that the sample was heated above  $T_C$ . Importantly, the chirality of skyrmionic bubbles could be reversed from CW to CCW (see Fig. 2c) if the sample was heated up and cooled down under applied positive electric field (36 mV/nm) and 11 mT magnetic field. This underscores that the presence of nonzero DMIs is required during formation of skyrmionic bubbles for chirality selection.

To reduce current through the sample under high external electric fields, we fabricated a FLG/ $h$ BN/CGT/FLG heterostructure and performed LTEM imaging *in situ* during the field cooling processes (Supplementary Videos S1-S2 and Figs. S4-S5). In Figs. 2d-h, LTEM images are shown, obtained after different field cooling processes, with electric fields applied ranging from -44 mV/nm to +37 mV/nm. The presence of the  $h$ BN layer enables application of a broader

range of electric fields without heating or damage induced by leakage current. A substantial negative electric field of  $-44$  mV/nm (Fig. 2d) predominantly induced CCW skyrmionic bubbles. When a positive electric field of  $+37$  mV/nm was applied, only CW skyrmionic bubbles were observed, as shown in Fig. 2h, confirming the chirality dependence on the electric field direction. With intermediate electric fields, both CCW and CW skyrmionic bubbles coexist after the field cooling. In Fig. 2i, we quantify the percentage of CCW skyrmionic bubbles in a wide field of view (Fig. S6) as a function of electric field, obtaining a linear dependence on external electric field. We observe a nearly random chirality (50% CCW and 50% CW) under  $-18$  mV/nm. This electric field offset may be attributed to an electron-beam-induced charging in the sample: in TEM, electron transparent samples, especially if insulating, are often positively charged by secondary and/or Auger electron emission.<sup>25</sup> Thus, the 500 nm thick silicon nitride substrate is likely positively charged under electron beam illumination, resulting in a net positive electric field.

The electric-field-induced chirality of skyrmionic bubbles was stable even with the electric field fully turned off and magnetic field reduced to 11 mT. Figs. 2j-k show two LTEM images obtained before and after increasing the magnetic field from 11 mT to 113 mT after a field cooling with  $-18$  mV/nm electric field and 50 mT magnetic field. Note that although the increase of magnetic field makes skyrmionic bubbles shrink, their LTEM contrast remains the same. This indicates that the vorticity and polarity, and thus the chirality, are preserved against variations in magnetic field.

To understand the microscopic origin of chirality selection, we conducted density functional theory (DFT) calculations using SIESTA-TB2J<sup>26</sup> with a focus on DMIs in the CGT under external electric fields. The magnetic  $\text{Cr}^{3+}$  ions in the edge-shared Te octahedra are arranged in a honeycomb lattice. Considering the honeycomb lattice as two interdigitated triangular lattices,



there are two distinguishable Cr sites. In our DFT study, we identified two primary DMIs: nearest neighbor (NN) and next nearest neighbor (NNN). In the absence of an electric field, the NN interactions involving two  $\text{Te}^{2-}$  anions do not exhibit a net DMI due to the centrosymmetric interaction pathway, as schematically shown in Fig. 3a. When an electric field is applied, the insulating CGT crystal becomes polarized by ionic displacements and/or electronic polarization. In a simple ionic charge screening scenario, the  $\text{Cr}^{3+}$  cations move along the electric field direction while the  $\text{Te}^{2-}$  anions shift in the opposite direction, resulting in the shortening of two Cr-Te bonds and the stretching of the other two. In Fig. 3a-c, the stretched Cr-Te bond lengths are indicated with gray lines. These ionic displacements break the inversion symmetry in the NN interaction pathway, resulting in nonzero DMIs. The primary components of electric-field-induced NN DMIs are in-plane and perpendicular to the nearest Cr-Cr bonds (see Table S1 in the Supplementary Information). In Figs. 3b and 3c, we show the calculated NN DMIs induced by negative and positive electric fields ( $\pm 2 \text{ V/\AA}$ ), respectively, for two Cr sites in the honeycomb lattice. Similar electric-field-induced DMI vector patterns have been calculated for  $\text{CrI}_3$  crystals, which have a honeycomb lattice of Cr in the edge-shared I octahedra.<sup>17</sup> A structural distinction between CGT and  $\text{CrI}_3$  lies in the presence of the Ge dimer at the center of the Cr honeycomb lattice, which does not significantly influence exchange interactions. We found that the vector sums of in-plane components of NN DMIs are relatively small while the vector sum of out-of-plane components remains non-zero:  $+0.0737 \text{ meV}$  and  $-0.0730 \text{ meV}$  (Table S1) for negative and positive electric fields, respectively. Note that the resultant out-of-plane components of NN DMIs align with the applied electric field direction and consequently change their sign when the electric field direction is reversed, as shown in Fig. 3d. This vector sum of out-of-plane components of NN DMIs dictates the rotation sense of in-plane magnetic spins within the Bloch domain walls. Considering the DMI

energy term  $-D_{ij} \cdot (S_i \times S_j)$ , CCW and CW spin arrangements are energetically favored for negative and positive electric fields, respectively, consistent with our experimental observations and micromagnetic simulations (Fig. 1e). According to our DFT calculations, the magnitude of the total NN DMIs is linearly scaled with the magnitude of electric field (see Fig. S7b). Consequently, the chirality response is linear with the magnitude of the external electric field, demonstrated in Fig. 2i. The magnitude of electric fields applied in our DFT calculations exceeds those employed in the experiments by two orders of magnitude (Fig. 2). This difference suggests that the resultant electric-field-induced DMIs in experiments are not strong enough to alter the chirality of pre-existing skyrmionic bubbles. However, they may be potent enough to influence chirality selection at the onset of skyrmionic bubble formation during the field cooling process. We rule out the effects of NNN DMIs on the skyrmion chirality as all NNN DMI vectors cancel each other regardless of the electric field direction (see Figs. 3b - c and Table S1).

In Fig. 4, we present LTEM images showing the skyrmionic bubble formation process during electric and magnetic field cooling. Near the phase transition, the spin-spin correlation length diverges, leading to the fluctuation of magnetic skyrmionic bubbles with varying diameters in both time and space. In the initial stage, at  $\sim 54$  K which is slightly below the  $T_C$ , small diameter skyrmionic bubbles are prominent, as depicted in Fig. 4e (see also Supplementary Videos 1-2 and Figs. S4-S5). These small skyrmionic bubbles undergo dynamic formation and annihilation processes down to 35 K. For example, we observed CCW and CW skyrmionic bubbles merge into a CW bubble, as shown in Figs. 4b-c. The average radius gradually increases from  $\sim 67$  nm to  $\sim 77$  nm with decreasing temperature. Due to the external magnetic field of 50 mT applied during the cooling process, formation of bubbles with large sizes may be suppressed, leading to the narrow size distribution. Upon further cooling, we observed continuous fluctuations in the bubble-bubble

pair distance between neighboring skyrmionic bubbles down to 15 K, as shown in Fig. 4f. Overall, the *in situ* LTEM imaging therefore provides direct observation of topologically nontrivial skyrmionic bubble formation and their evolution during magnetic phase transitions.

In conclusion, we studied the effect of electric field on the chirality of skyrmionic bubbles in 2D vdW CGT. By direct imaging of skyrmionic bubble formation across the phase transition, we demonstrated control of skyrmionic bubble chirality via the electric field direction during magnetic field cooling. The resulting bubbles and their chirality remained stable at low temperatures, even with variations in applied magnetic and electric fields. The proportion of skyrmionic bubbles in the CW to CCW configuration exhibited a linear scaling with the electric field magnitude, in measurements that were facilitated by the insertion of a current-blocking *h*BN layer. According to DFT calculations, the collective vector sum of NN DMIs predominantly aligns in the out-of-plane direction. This orientation undergoes a reversal in polarity when the direction of the electric field is altered, thus playing a pivotal role in the chirality selection. Our study demonstrates that external electric fields, when applied along the out-of-plane direction, can control the in-plane spin chirality of nonmetallic 2D vdW magnets. The electric field control of skyrmionic bubble chirality in this study paves the way for the development of future topological spintronic and quantum computing devices utilizing topological spin textures in 2D vdW magnets.

## **Methods**

### **Crystal growth**

$\text{Cr}_2\text{Ge}_2\text{Te}_6$  was synthesized using a tellurium flux in a quartz glass ampoule. A quartz ampoule ( $25 \times 100$  mm) was loaded with a 50 g mixture corresponding to the composition  $\text{Cr}_2\text{Ge}_2\text{Te}_{10}$ . The mixture consists of Cr powder (99.99%, -60 mesh, Chemsavers, USA), germanium granules

(99.9999%, 2-6 mm, Wuhan Xinrong New Material Co., China) and tellurium (99.9999%, 2-6 mm, Wuhan Xinrong New Material Co., China). The loaded ampoule was sealed under high vacuum ( $<1 \times 10^{-3}$  Pa using diffusion pump and liquid nitrogen trap) using a hydrogen-oxygen torch. The sealed ampoule was placed in a muffle furnace horizontally and heated to 1000 °C at a heating rate of 1 °C/min. The ampoule was held at 1000 °C for 12 hours to ensure thorough reaction. To ensure homogeneity of the melt, the ampoule was mechanically shaken several times while maintained at 1000 °C in the furnace. After that, the temperature was gradually reduced to room temperature at a cooling rate of 6 °C/hour. The sealed ampoule was opened in an argon-filled glovebox. The plates of up to 10 mm in lateral dimensions were mechanically separated from the middle section of the ingot.

### **TEM sample and device fabrication**

FLG/CGT/FLG or FLG/hBN/CGT/FLG heterostructures were fabricated using conventional dry transfer methods based on a polycarbonate (PC) stamp<sup>27</sup>. CGT and graphene were exfoliated from bulk crystals onto 90 nm SiO<sub>2</sub>/Si substrates. Suitable flakes were selected based on optical contrast. For graphene, we aimed for few-layer graphene flakes with a thickness of 3-10 layers. For CGT, we aimed for bulk CGT with a shiny, golden surface. The finished heterostructures were transferred to custom-fabricated TEM grids (Norcada, Inc, Canada) using wedging transfer<sup>28</sup>. For this, the SiO<sub>2</sub>/Si substrate was spin coated with a solution of cellulose acetate butyrate (CAB) dissolved in ethyl acetate. This polymer was used as a handle during the transfer. The CAB with heterostructure attached to it was transferred by hand to the TEM grid, baked to 80 °C to improve adhesion, and the CAB was dissolved in acetone.

## ***In situ* cryogenic TEM experiments**

We used a customized liquid-helium cooling TEM holder (HCTDT3010, Gatan Inc.) with four electrodes for *in situ* biasing experiments. Electrical contacts were made by wire bonding. A double spherical-aberration-corrected JEOL ARM200CF at Brookhaven National Laboratory was used to perform LTEM imaging with a direct electron detector (K3, Gatan, Inc.). The standard objective lens excitation was used to apply external magnetic fields. Magnetic fields at the sample position were measured with a custom-made four-point probe TEM holder for each lens value used in this study. A source meter unit (SMU2600B, Tektronix) was used to apply external bias to the TEM sample and to measure the current flowing through the samples.

## **Density functional theory calculations**

First-principles calculations using density functional theory (DFT) plus  $U$  level with spin-orbit coupling of a CGT monolayer were performed using SIESTA<sup>29</sup>.  $U = 0.5$  eV was used and electric fields of  $\pm 2$  V/Å were applied to acquire the DMI vectors at positive and negative electric fields. The magnetic exchange interactions were calculated according to the following Heisenberg exchange function using TB2J<sup>26</sup>

$$E = - \sum_i K_i^{SIA} S_i^2 - \sum_{i \neq j} [J_{ij}^{ISO} S_i \cdot S_j + S_i J_{ij}^{ANI} S_j + D_{ij}^{DMI} \cdot (S_i \times S_j)]$$

where  $K_i^{SIA}$  is the single ion anisotropy,  $J_{ij}^{ISO}$  is the isotropic exchange interaction,  $J_{ij}^{ANI}$  is the anisotropic exchange interaction,  $D_{ij}^{DMI}$  is the DMI,  $S_i$  and  $S_j$  are the unit vector of the spin moment at the sites  $i$  and  $j$ , respectively. The vector sum of the three NN DMIs for positive and negative applied electric fields were -0.0730 meV and 0.0737 meV respectively.

## **Data analysis**

We binned the raw LTEM data from  $3,456 \times 3,456$  pixels to a size of  $432 \times 432$  pixels. We then denoised the binned image using the BM3D algorithm<sup>30</sup>, a real-space denoising method that uses clustering and block matching. Finally, we applied a real-space 2D Gaussian smoothing to the BM3D denoised image as fine smoothing. The magnetic chirality, radius and centers of the skyrmionic bubbles are found by a circular Hough transform based algorithm of MATLAB<sup>31</sup>.

### **Micromagnetic and LTEM image simulations**

We performed micromagnetic simulations using Mumax<sup>3</sup> for a sample dimension of  $256 \times 256 \times 8$  nm<sup>3</sup> with the following material parameters: saturation magnetization ( $M_{\text{sat}}$ )  $1.37 \times 10^5$  A/m, exchange stiffness ( $A_{\text{ex}}$ )  $1.21 \times 10^{-12}$  J/m, uniaxial anisotropy ( $K_{\text{u1}}$ )  $3.6 \times 10^4$  J/m<sup>3</sup>, DMI density  $\pm 1.25 \times 10^{-4}$  J/m<sup>2</sup>, and external B field strength applied in the out-of-plane direction 7 mT. The cell size was 2 nm. For LTEM image simulation, we used PyLorentz<sup>32</sup> with defocus value  $+2$   $\mu\text{m}$  and electron energy 200 keV.

### **Data availability**

The data that support the plots within this paper and other findings of this study are available from the corresponding author upon reasonable request.

### **Reference:**

1. Tokura, Y. and Kanazawa, N. Magnetic skyrmion materials. *Chemical Reviews* 121, 2857-2897 (2021).
2. Marrows, C.H. and Zeissler, K. Perspective on skyrmion spintronics. *Applied Physics Letters* 119, 250502 (2021).
3. Wang, Q.H. et al. The magnetic genome of two-dimensional van der Waals materials. *ACS Nano* 16, 6960-7079 (2022).
4. Fert, A., Reyren, N. and Cros, V. Magnetic skyrmions: advances in physics and potential applications. *Nature Reviews Materials* 2, 17031 (2017).

5. Gibertini, M. et al. Magnetic 2D materials and heterostructures. *Nature Nanotechnology* 14, 408 (2019).
6. Avsar, A. et al. Spintronics in graphene and other two-dimensional materials. *Reviews of Modern Physics* 92, 021003 (2020).
7. Kurebayashi, H. et al. Magnetism, symmetry and spin transport in van der Waals layered systems. *Nature Review Physics* 4, 150-166 (2022).
8. Han, M.-G. et al. Topological magnetic-spin textures in two-dimensional van der Waals  $\text{Cr}_2\text{Ge}_2\text{Te}_6$ . *Nano Letters* 19, 7859-7865 (2019).
9. Park, T.-E. et al. Néel-type skyrmions and their current-induced motion in van der Waals ferromagnet-based heterostructures. *Physical Review B* **103**, 104410 (2021).
10. Wu, Y. et al. Néel-type skyrmions in  $\text{WTe}_2/\text{Fe}_3\text{GeTe}_2$  van der Waals heterostructure. *Nature Communications* 11, 3860 (2020).
11. Nagaosa, N. and Tokura, Y. Topological properties and dynamics of magnetic skyrmions. *Nature Nanotechnology* 8 (12), 899-911 (2013).
12. Tokunaga, Y. et al. A new class of chiral materials hosting magnetic skyrmions beyond room temperature. *Nature Communications* 6, 7638 (2015).
13. Sierra, J. F. et al. Van der Waals heterostructures for spintronics and opto-spintronics. *Nature Nanotechnology* 16, 856-868 (2021).
14. Verzhbitskiy, I. and Eda, G. Electrostatic control of magnetism: Emergent opportunities with van der Waals materials. *Applied Physics Letters* 121, 060501 (2021).
15. Fillion, C.-E. et al. Gate-controlled skyrmion and domain wall chirality. *Nature Communications* 13, 5257 (2022).
16. Psaroudaki, C., Peraticos, E., and Panagopoulos, C., Skyrmion qubits: Challenges for future quantum computing applications, *Appl. Phys. Lett.* 123, 260501 (2023).
17. McGuire, M. A. et al. Coupling of crystal structure and magnetism in the layered, ferromagnetic insulator  $\text{CrI}_3$ . *Chemistry of Materials* 27, 612-620 (2015).
18. Liu, J. et al. Analysis of electric-field-dependent Dzyaloshinskii-Moriya interaction and magnetocrystalline anisotropy in a two-dimensional ferromagnetic monolayer. *Physical Review B* 97, 054416 (2018).
19. Behera, A. K., Chowdhury, S., and Das, S. R. Magnetic skyrmions in atomic thin  $\text{CrI}_3$  monolayer. *Applied Physics Letters* 114, 232402 (2019).
20. Gong, C. et al. Discovery of intrinsic ferromagnetism in two-dimensional van der Waals crystals. *Nature* 546, 265-269 (2017).
21. Li, C.-K., Yao, X.-P., and Chen, G. Writing and deleting skyrmions with electric fields in a multiferroic heterostructure. *Physical Review Research* 3, L012026 (2021).
22. Verbitsky, I. A. et al. Controlling the magnetic anisotropy in  $\text{Cr}_2\text{Ge}_2\text{Te}_6$  by electrostatic gating. *Nature Electronics* 3, 460-465 (2020).
23. Jiang, N. et al. Electric current control of spin helicity in an itinerant helimagnet. *Nature Communications* 30, 1601 (2020).
24. McCray, A. R. C., et al. Direct observation of magnetic bubble lattices and magnetoelastic effects in van der Waals  $\text{Cr}_2\text{Ge}_2\text{Te}_6$ . *Advanced Functional Materials* 33, 2214203 (2023).
25. Reimer, L. Image formation in low voltage scanning electron microscopy pp. 71 - 135. SPIE Press, Bellingham (1993).
26. He, X. et al., TB2J: a python package for computing magnetic interaction parameters. *Computer Physics Communications*, 107938 (2021).

27. Zomer, P. J., et al. "Fast pick up technique for high quality heterostructures of bilayer graphene and hexagonal boron nitride." *Applied Physics Letters* 105, 1 (2014).
28. Schneider, Grégory F., et al. "Wedging transfer of nanostructures." *Nano letters* 10, 5 (2010). 1912-1916.
29. Soler, J. M. et al. The SIESTA method for ab initio order-N materials simulation, *J. Phys. Condens. Matter* **14**, 2745(2002)
30. Dabov, K., Foi, A., Katkovnik, V., and Egiazarian, K., Image Denoising by Sparse 3-D Transform-Domain Collaborative Filtering. *IEEE Transactions on Image Processing* 16, 2080-2095 (2007)
31. Yuen, H.K., Princen, J., Illingworth, J., and Kittler, J., Comparative study of Hough transform methods for circle finding. *Image and vision computing* 8, 71-77 (1990).
32. McCray, A.R.C., et al. Understanding complex spin textures with simulation-assisted Lorentz transmission electron microscopy, *Phys. Rev. Appl.* 15, 044025 (2021).

## **Acknowledgments**

The work at the Brookhaven National Laboratory was supported by the U.S. Department of Energy (DOE), Basic Energy Sciences, Materials Science and Engineering Division, under Contract DESC0012704. This research used Electron Microscopy resources of the Center for Functional Nanomaterials (CFN), which is a U.S. DOE Office of Science User Facility, at Brookhaven National Laboratory under Contract DESC0012704. The work at MIT was primarily supported through the Department of Energy BES QIS program on "Van der Waals Reprogrammable Quantum Simulator" under award number DE-SC0022277 and partially supported by the Quantum Science Center (QSC), a National Quantum Information Research Center of the U.S. Department of Energy (DOE) on probing quantum matter. P.N. gratefully acknowledges support from the John Simon Guggenheim Memorial Foundation (Guggenheim Fellowship) as well as support from a NSF CAREER Award under Grant No. NSF-ECCS-1944085. Z.S. was supported by ERC-CZ program (project LL2101) from Ministry of Education Youth and Sports (MEYS) and used large infrastructure from project reg. No. CZ.02.1.01/0.0/0.0/15\_003/0000444 financed by the EFRR.

## **Author contributions**



M.-G.H. and J.D.T. conceived the research. L.D. and J.S. synthesized and characterized the crystals. J.D.T. designed and fabricated heterostructure samples. F.C. contributed to electrical connection to the TEM samples and transport measurements of them. M.-G.H. and J.D.T., performed *in situ* TEM experiments. J.P.P., E.P. and P.N. carried out the DFT calculations. C.L. performed the micromagnetic and LTEM simulations. M.-G.H., J.D.T. and J.M. processed and analyzed data. F.M.R., P.N., and Y.Z. supervised the research. M.-G.H. wrote the paper with key contributions from J.D.T., E.P. F.M.R., and Y.Z. The manuscript reflects the contributions and ideas of all authors.

### **Competing interests**

The authors declare no competing interests.

### **Additional information**

**Correspondence and requests for materials** should be addressed to Myung-Geun Han.

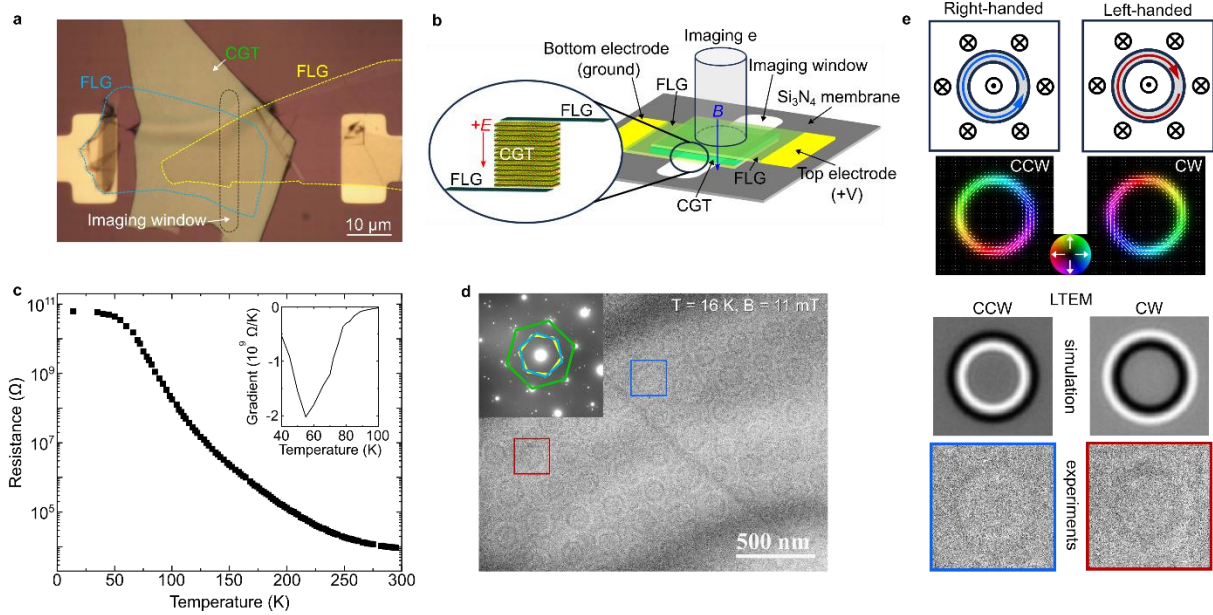


**Fig. 1 | Heterostructure of FLG/Cr<sub>2</sub>Ge<sub>2</sub>Te<sub>6</sub> (CGT)/FLG for *in situ* biasing experiments and random chirality in skyrmionic bubbles.** **a**, An optical image of the FLG/CGT/FLG heterostructure on a custom-designed 500 nm thick silicon nitride membrane with a 4 μm x 34 μm observation window and two 50 nm thick Cr/Pt electrodes. Note that the CGT is sandwiched between two FLG layers contacted to the bottom and top Cr/Pt electrodes. **b**, A schematic of the device showing the direction of external electric and magnetic fields. The magnetic field in the imaging direction was controlled by the objective lens. **c**, Resistance vs. temperature data measured from the fabricated TEM sample. The inset shows the gradient of resistance as a function of temperature, which shows an upturn near 55 K. **d**, LTEM image showing skyrmionic bubble lattices obtained at T = 16 K and 11 mT magnetic field after the sample was cooled in a 50 mT field without an electric field. The defocus value was about +300 μm. The inset shows the electron diffraction pattern of the device. The diffraction spots from the two FLG layers (yellow and blue) and the CGT (green) are marked. **e**, Schematics of magnetic spin configuration of skyrmionic bubbles with right-handed and left-handed chirality and their in-plane spin configurations simulated by micromagnetic simulation (top panel). In order to induce the CCW bubble, a bulk DMI energy density of  $-1.25 \times 10^{-4} \text{ J/m}^2$  was applied while the CW bubble was induced by  $+1.25 \times 10^{-4} \text{ J/m}^2$  (the sign convention is the same as the electric field direction). The color wheel represents the direction and magnitude of in-plane spin components. Simulated LTEM image contrast and experimental LTEM images of skyrmionic bubbles with opposite chirality are shown in the bottom panel.

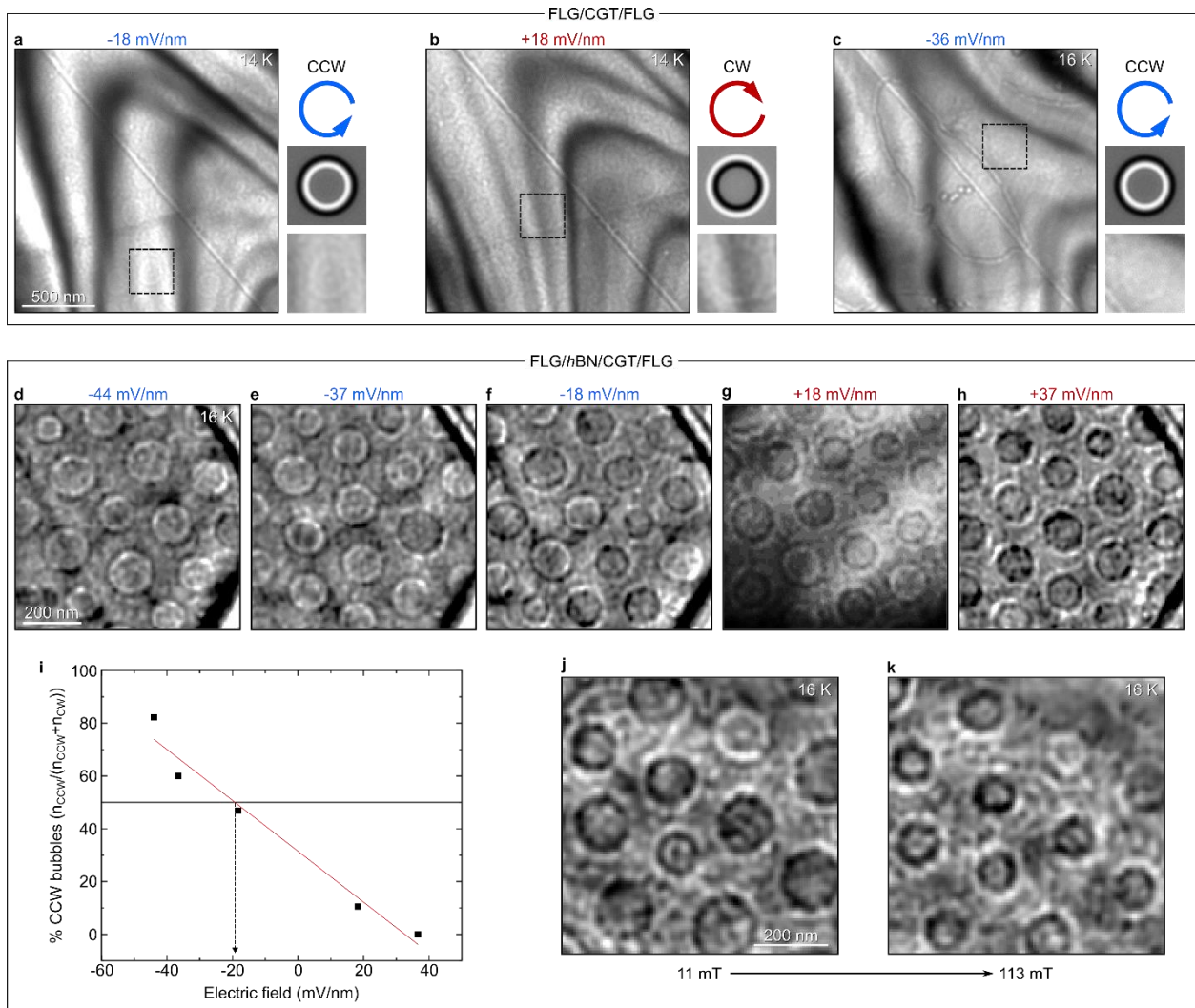


**Fig. 2| Electric field control of chirality in skyrmionic bubbles.** **a-b**, LTEM images (approx. 300  $\mu\text{m}$  overfocus) of FLG/CGT/FLG heterostructure obtained after cooling in  $\pm 18$  mV/nm electric field and 50 mT magnetic field. **c**, LTEM image after poling the skyrmionic bubbles shown in **b** with large negative electric field (-36 mV/nm) at  $T = 16$  K. Damaged parts of FLG layers can be seen. Domain structures, completely changed from **b**, show stripes and skyrmionic bubbles with reversed chirality (from CW in **b** to CCW in **c**) in the CGT layer. It should be noted that the LTEM images shown in **a** and **b** are obtained with the same + 300  $\mu\text{m}$  overfocus condition. **d-h**, LTEM images (approx. 200  $\mu\text{m}$  overfocus) of FLG/hBN/CGT/FLG heterostructure obtained after various electric field cooling. The skyrmionic bubble chirality induced by electric field is consistent with the results in **a** and **b**. **i**, Relative population of white and bright skyrmionic bubbles as a function of electric field during field cooling. **j-k**, Two LTEM images obtained after electric field 18 mV/nm under two different magnetic fields, 11 mT (left) and 113 mT (right) showing no change in bubble contrast hence no change in polarity (core spin direction).

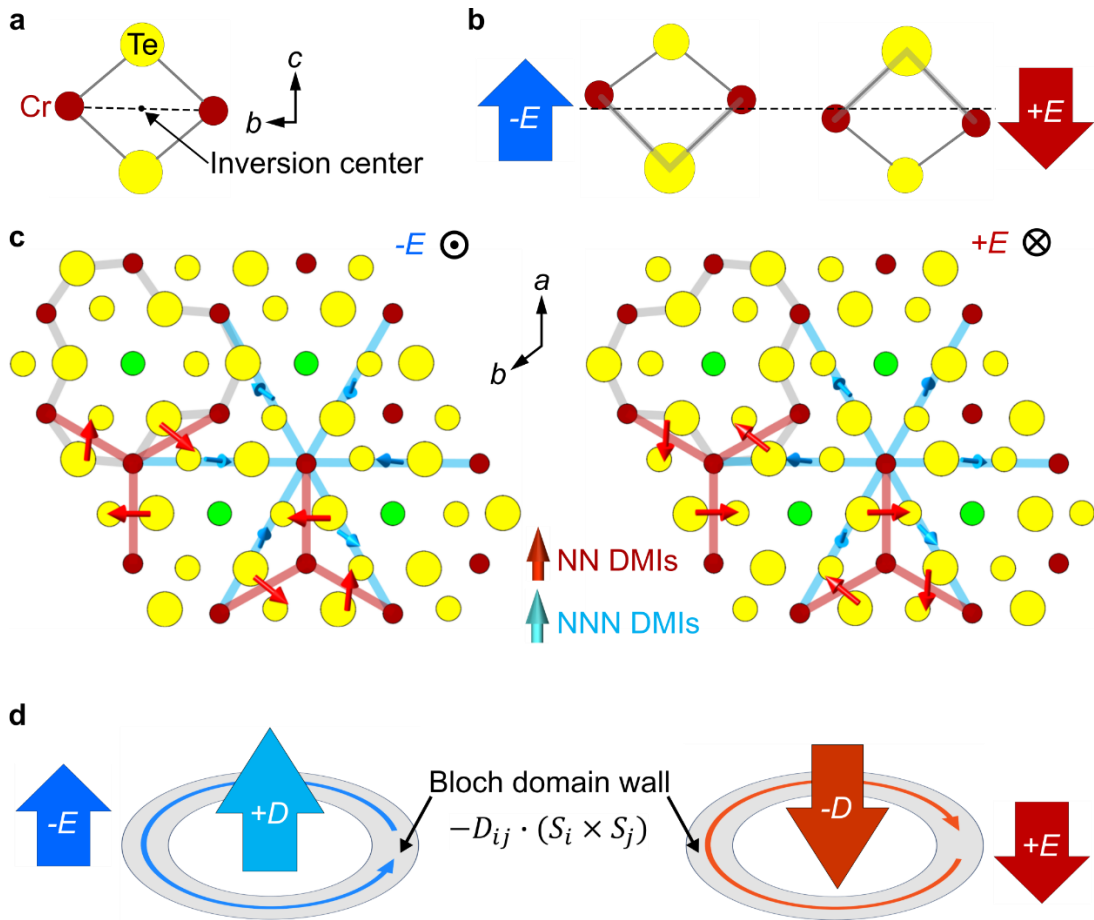


**Fig. 3| DMI vector patterns under external electric fields.** **a**, An atomic model showing the NN pathway under zero electric field. An inversion center is at the midpoint between two interacting Cr ions. **b**, Atomic models of the NN pathways under negative and positive electric fields, respectively. Ionic displacements are exaggerated for visualization. The stretched Cr-Te bonds are highlighted with gray lines. **c**, DMI patterns in the honeycomb lattice under negative (left) and positive (right) electric fields. The light blue arrows represent NNN DMIs along the NNN pathways highlighted with the light blue lines. The red arrows represent NN DMIs for two Cr sites with the NN pathways highlighted with the red lines. The gray lines highlight the stretched Cr-Te bonds due to ionic displacements. The Te ions in the stretched bonds are enlarged for visualization. **d**, Schematics of in-plane spin arrangements within the Bloch domain walls under negative (left) and positive (right) electric fields. The vector sums of out-of-plane components of the NN DMIs are indicated with the blue and red arrows.

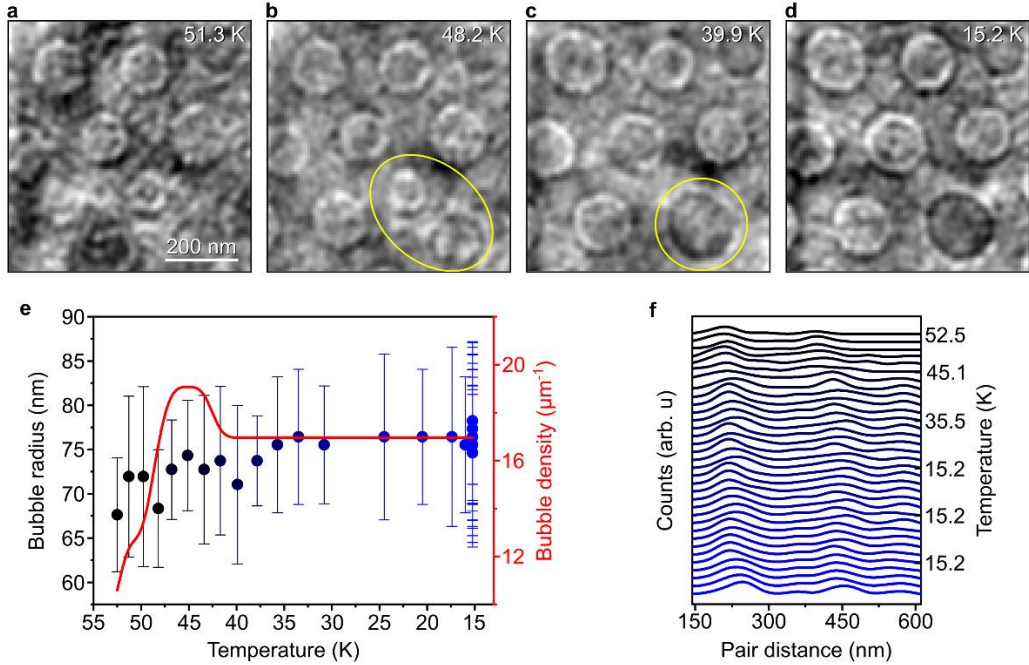


**Fig. 4| Chirality-selected bubble formation under field cooling.** **a-d**, A temperature series of LTEM images obtained during negative electric field (-37 mV/nm) cooling. The magnetic field during cooling was 50 mT. From 48.2 K (**b**) to 39.9 K (**c**), CW and CCW bubbles (circled in **b**) merge into a CCW bubble (circled in **c**). **e**, Bubble radius and bubble density as a function of temperature during field cooling. The data points were extracted from LTEM images. Small bubbles are first observed, and then average bubble size becomes uniform on further cooling down. The density of bubbles rapidly increases in the beginning before converging to  $\sim 17$  bubbles/ $\mu\text{m}^2$ . **f**, The pair distance measurements across field cooling.